PHYSICAL REVIEW B **105**, 235416 (2022)

Reversible switching of anomalous valley Hall effect in ferrovalley Janus 1*T*-CrO*X* (X = F, Cl, Br, I) and the multiferroic heterostructure CrO*X*/In_2Se_3

R. J. Sun,[1] R. Liu,[1] J. J. Lu,[1] X. W. Zhao,[1] G. C. Hu,[1] X. B. Yuan,[1] and J. F. Ren[1,2,*]

[1] *School of Physics and Electronics, Shandong Normal University, Jinan, 250358, China*
[2] *Shandong Provincial Engineering and Technical Center of Light Manipulations & Institute of Materials and Clean Energy, Shandong Normal University, Jinan 250358, China*

(Received 28 March 2022; accepted 1 June 2022; published 10 June 2022)

The central issue for practical applications of the anomalous valley Hall effect (AVHE) is the tunable and nonvolatile nature of the valley splitting. We predict a type of ferrovalley material, Janus 1*T*-CrO*X* (X = F, Cl, Br, I), in which the switching effect of the AVHE can be achieved by adjusting the biaxial strain or building a multiferroic heterostructure CrO*X*/In_2Se_3. Stable out of plane magnetization in CrO*X* induces the valley splitting which can reach to 112 meV in the CrOBr monolayer. Interestingly, we find that the valley splitting of CrOCl is robust against the biaxial strain both in the conduction band and the valence band. In contrast, the valley splitting of the CrOBr at the conduction band can be linearly modulated, while it has a switching response at the valence band due to the strong orbital hybridization induced by compressive strain, so a reversible switch of the AVHE can be achieved. Furthermore, the electric reversible valley splitting switch is also obtained in multiferroic van der Waals heterostructure CrOCl/In_2Se_3, and the reversible switch of the AVHE can also be manipulated by controlling the polarization states of the ferroelectric layer. The AVHE in CrO*X* can be readily switched on or off by either applying biaxial strain or reversing the ferroelectric polarization of the substrate In_2Se_3, which may be a promising application in the field of valleytronics.

DOI: 10.1103/PhysRevB.105.235416

I. INTRODUCTION

The valley, a new degree of freedom, is the energy extreme of the band dispersion in two-dimensional (2D) materials, regarded as pseudospin. It is embodied in two or more energy degenerated but unequal valleys at the corners of the Brillouin zone, whose binary states lay the foundation for valleytronic devices in functional applications, such as storing information and performing logical operations [1–4]. Following the study of valleytronics on 2D graphene and transition metal disulfides, interesting phenomena such as the valley Hall effect and valley-dependent optical selection rules have been demonstrated, and subsequently applications based on valley degrees such as valley spin valves and valley filters have been predicted theoretically and achieved experimentally [5–8].

The further applications of valley signals and the development of valleytronics for binary information coding and storage are restricted by valley degeneracy. Therefore, people have successively proposed various strategies to obtain the valley splitting by breaking the time-reversal symmetry, including external electromagnetic fields, optical pumps, magnetic doping, or magnetic proximity effects [9–14]. However, some of the above methods are volatile and difficult to control, and some of them will introduce impurity scattering or produce very small values of valley splitting, which are not conducive to practical applications in valleytronics [10,14]. Importantly, it is experimentally difficult to get valley splitting either by external means or by using magnetic substrates. Therefore, the central issue for practical applications of valleytronic devices remains the tunable and the nonvolatile nature of the valley splitting.

It is necessary to find the strategies to obtain intrinsic valley splitting materials. Inspired by the magnetic proximity effect, the coupled interactions of the intrinsic magnetic exchange field with the spin-orbit coupling is by far the most desirable way to obtain the nonvolatile intrinsic valley splitting. Spatial and the time-reversal asymmetry lead to a nonzero valley magnetic moment and the Berry curvature at the valley has unequal size and opposite sign, so valley splitting appears. When a transverse voltage is applied, Bloch electrons acquire anomalous velocities and the anomalous valley Hall effect (AVHE) is generated. The intrinsic magnetic exchange field and the spin-orbit coupling coexist in ferromagnetic semiconductors, so generation of nonvolatile valley splitting as well as the AVHE in them are hot topics in valleytronics research. Therefore, a number of explorations of valleys have emerged in numerous 2D materials, including graphene, transition metal disulfides, antiferromagnetic post-transition metal compounds, and lanthanide compounds [5,6,15,16]. Meanwhile, some intrinsic ferrovalley (FV) materials also have been gradually proposed, such as $FeCl_2$, GdI_2, NdX_2, etc. [17–19]. However, most of the reported intrinsic FV materials are in the *H* phase, while the Janus materials in the *T* phase are very rare. Inspired by the above studies, we hypothesize that 2D magnetic *T*-phase Janus materials can be found to break their valley degeneration and retain piezoelectricity, and can act as FV materials for various nanoelectronic device

---

[*] renjf@sdnu.edu.cn

applications. Meanwhile, the in-plane and the mirror asymmetry of Janus materials induce various properties, such as valley splitting, magnetic anisotropy effect, and even strong Rashba effect, and there has been a proliferation of research works on them [20–22]. Importantly, the structural asymmetry of the Janus materials produces piezoelectric properties, and the built-in electric field can have a significant impact on the valley properties. These properties are conducive to further tune the valley degree by using interlayer van der Waals (vdW) interaction, and the flexible tunability of valley signals provides a platform for the applications of valleytronic devices [23–25].

In this paper, we successfully predict the FV materials, Janus 1*T*-CrO*X* (X = F, Cl, Br, I) monolayers, and a huge valley splitting of 112 meV can be achieved due to the coexistence of the spin-orbit coupling and the local $3d$ electrons of Cr atoms. Based on the first principle, our calculations show that when the Berry curvatures at the valleys are of opposite signs and different sizes in these systems, the AVHE occurs [26–28]. Then, we modulate the valley splitting in 1*T*-CrO*X* by applying strain, changing the U values of the Cr atoms, and changing the magnetization directions. Importantly, the valley splitting of CrOBr has a switching response at the valence band when compressive strain is applied, so a reversible switch of the AVHE can be achieved. Meanwhile, the valley splitting of 1*T*-CrO*X* varies as a cosine function of the magnetization direction, which is consistent with the constructed Hamiltonian quantities and the derived formula. We also build multiferroic vdW heterostructures CrO*X*/In_2Se_3 and the reversible switch of the AVHE can also be manipulated by controlling the polarization states of the ferroelectric (FE) layer [29–32]. We hope that our results provide a promising platform to exploit valleytronic applications.

II. COMPUTATIONAL METHOD

First-principles calculations based on density functional theory (DFT) are performed by the projector augmented wave (PAW) method implemented in the Vienna *ab initio* simulation package (VASP) [33,34]. The generalized gradient approximation (GGA) of Perdew-Burke-Ernzerhof (PBE) parametrization is used for the exchange correlation potential [35,36]. A vacuum layer in the z direction with a thickness of 20 Å is set to ensure decoupling between the periodic layers. A Γ-centered Monkhorst-Pack grid of 15 × 15 × 1 is employed to perform the first Brillouin zone integral [37]. A 600 eV energy cutoff is adopted to expand the wave functions. All the atoms are allowed to relax until the atomic force on each atom is smaller than 0.01 eV/Å. The screened exchange hybrid density functional of Heyd-Scuseria-Ernzerhof (HSE) is employed to obtain accurate electronic structures [38]. In addition, the electronic structures are calculated with the spin-orbit coupling [39]. To confirm the results, the calculations are also checked with a PBE $+U$ method, in which Coulomb interaction U terms are considered for the Cr $3d$ orbital [40]. The total energy is converged to within 10^{-6} eV. The vdW interaction correction is considered through the DFT-D3 method [41]. Phonon spectra are calculated by using the DFT perturbation theory [42]. The Berry curvatures of CrO*X* are calculated by using the maximum local Wannier functions (MLWFs) implemented in the WANNIER90 package [43]. The Monte Carlo simulation based on spin Heisenberg model is performed by the VAMPIRE code [44].

III. RESULTS AND DISCUSSION

Figure 1(a) shows the crystal structures of monolayer 1*T*-CrO*X* (X = F, Cl, Br, I). They exhibit a hexagonal lattice with a space group of $p3m1$, which is formed by O-Cr-*X* misalignment stacking. According to the electronic coordination analysis, the Cr atoms transit from $4s^1 3d^5$ to $4s^0 3d^3$ in the electronic arrangement during the synthesis of compound 1*T*-CrO*X*, so theoretically they would have magnetic moments of 3 μB. Therefore, the spatial and time-reversal symmetry of 1*T*-CrO*X* would be broke by their unique Janus structure and their intrinsic magnetism, which will give rise to intrinsic valley splitting. Next, we calculate their structural and electronic properties. We find that CrOF, CrOCl, and CrOBr are indirect band gap semiconductors, while CrOI is metallic. Importantly, the valley degrees of freedom are found in CrOCl, CrOBr, and CrOI, and their band structures are shown in Fig. S1 of the Supplemental Material (SM) [45]. It is found that the band gaps decrease as the atomic number of the halogen elements increases. At the same time, the inherent ferromagnetic properties of the systems make the spin splitting very large; then the energy levels near the Fermi surface are occupied by a single spin-up carrier, so CrO*X* (X = F, Cl, Br) are half-semiconductors. The spin splittings in them are large

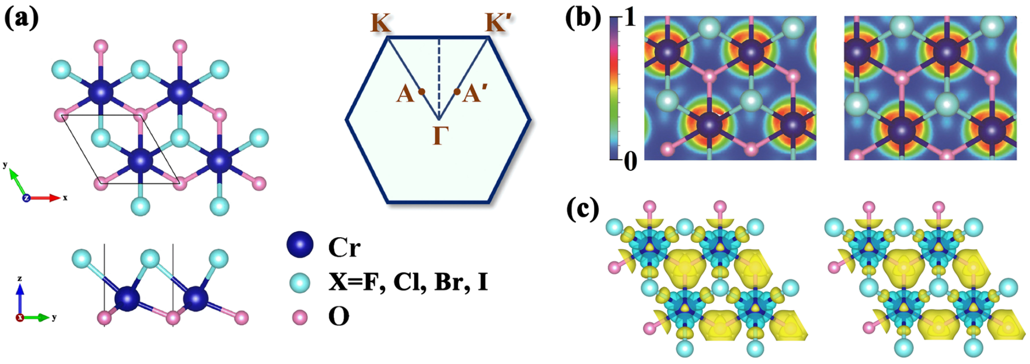

FIG. 1. (a) The crystal structures of 1*T*-CrO*X* (X = F, Cl, Br, I) from top and side views and the schematic diagram of the first Brillouin zone. (b) The electron localization function of CrOCl and CrOBr. (c) The differential charge densities of CrOCl and CrOBr.

enough to overcome the thermal noise, which is necessary for manipulation at room temperature.

The stabilities of 1*T*-Cr*OX* (X = Cl, Br, I) which carry valley signals are further verified. Firstly, we perform the calculations of the phonon dispersion spectrum and find that the phonon spectra of CrOCl, CrOBr are positive throughout the Brillouin zone, which proves their kinetic stability, while CrOI, on the contrary, is not stable. Next, we calculate the formation energy E_{form}, which is defined as $E_{\text{form}} = (3E_{\text{CrO}X} - \frac{1}{2}E_{\text{Cr}2X6} - 2E_{\text{CrO2}} + \frac{1}{2}E_{\text{O2}})/9$. Here, $E_{\text{CrO}X}$ is the total energy of the CrOCl or CrOBr, $E_{\text{Cr}2X6}$ is the total energy of Cr_2X_6, E_{CrO2} is the total energy of CrO_2, and E_{O2} is the total energy of O_2, respectively. The specific values are shown in Table S1 of the SM [45], and we find that their values are negative and comparable with that of the VI_3 monolayer (–0.89 eV) [46]. Finally, we calculate their elastic constants and find that they meet the elastic stability criteria (i.e., $C_{11} > 0$ and $|C_{12}| > 0$), proving their mechanical stability [47]. The phonon spectra and the elastic constants are shown in Fig. S2 and Table S2 of the SM [45]. The above calculations prove that the CrOCl, CrOBr systems are promising to be successfully synthesized and stabilized experimentally.

Next, we focus on the structures which are stable and pose valley properties, i.e., CrOCl and CrOBr. As shown in Fig. 1(b), the electron localization function shows that the electrons of CrOCl and CrOBr are mainly dispersed around the Cr, the Cl, or the Br atoms, indicating their ionic bonding characteristics. Meanwhile, the differential charge densities of the systems are shown in Fig. 1(c). The magnetic moments of the system are calculated, and it is found that they mainly originate from the Cr atom; the spin density distributions are shown in Fig. S3(a) of the SM [45]. To study the magnetic ground states of the monolayers CrOCl and CrOBr, we calculate the total energies of the ferromagnetic (FM) and the antiferromagnetic (AFM) configurations (as shown in Fig. S3(b) [45]). It is found that the energies of the FM states are lower than those of the AFM states, so FM configurations are the most stable ones. Therefore, the magnetic ground states of CrOCl and CrOBr are FM states. The fundamentals of the FM ground states of CrOCl and CrOBr are related to the superexchange interaction, where the Cr-*X*-Cr bonding angle is approximately equal to 90°. Based on the Goodenough-Kanamori-Anderson rule, the superexchange interaction will dominate the interaction between the Cr atoms, which leads to the FM coupling [48,49]. The magnetic moments of each atom (CrOCl and CrOBr) under biaxial strain are shown in Fig. S4 of the SM [45], and we can find that the magnetic moments of Cr and *X*/O atoms are antiparallel to each other, proving the existence of superexchange interactions. The easy magnetization axis is parallel to the z axis based on the calculated results in Table S3 [45]. The magnetic anisotropy energy is small, so it can be ignored; thus the spin Hamiltonian under the Heisenberg model can be written as

$$H = -\sum_{i,j} J\, S_i S_j \;, \tag{1}$$

where J is the nearest magnetic exchange coupling parameters, and S is the spin quantum number. The magnetic exchange coupling parameters can be calculated through the energy difference between the FM and the AFM configurations,

$$E_{\text{FM}} = E_0 - 6J|S|^2, \quad E_{\text{AFM}} = E_0 + 2J|S|^2. \tag{2}$$

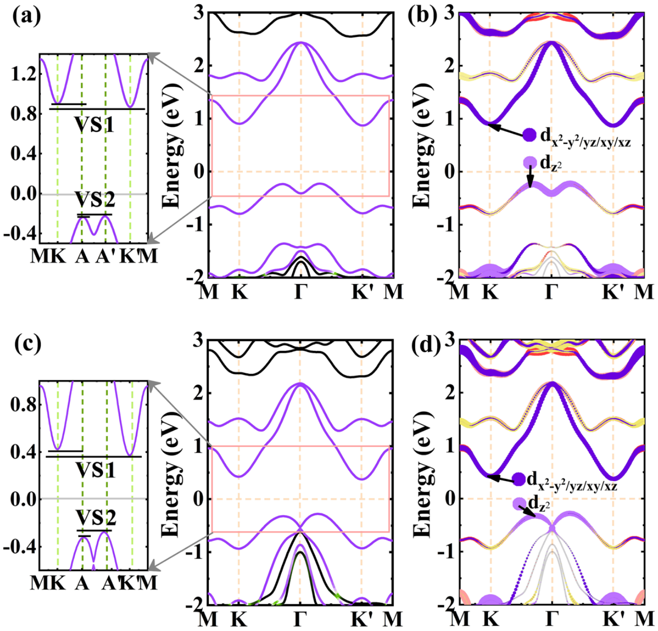

FIG. 2. (a), (b) are the band structures and the orbital-projected band structures under PBE for CrOCl with spin-orbit coupling, while (c), (d) are the cases for CrOBr.

As listed in Table S3 of the SM, the values of J of CrOCl and CrOBr are 2.56 and 0.61 meV, respectively, which means the systems favor the FM states. These results are consistent with the fact that the ground states of CrOCl and CrOBr are FM states based on the existence of the superexchange interaction. In addition, the FM coupling parameter J decreases with the increasing of the atomic number of the halogen elements. The superexchange coupling bridge will weaken with the increasing of the energy difference of the p orbitals between the halogen element and the O, so the J decreases. Next, we simulate the Curie temperature by Monte Carlo using the VAMPIRE code; the results are shown in Fig. S5 of the SM [45]. The calculated T_C of CrOCl and CrOBr monolayers are 85 and 17 K, respectively. Although such T_C are still below room temperature, they are higher or closer to some FM monolayers (for example, T_C = 45 K for CrI_3 [50]), so CrOCl and CrOBr are very promising for applications in valleytronic and spintronic devices.

We perform a systemic analysis about the valley properties of CrOCl and CrOBr. Firstly, the band structures with PBE after considering spin-orbit coupling are shown in Figs. 2(a) and 2(c), and we find that the spin-up and spin-down channels split significantly due to the large intrinsic magnetic moments. The conduction and the valence bands near the Fermi energy level are controlled by the spin-up channels, so both of them are half-semiconductors. Importantly, it is found that the valley splitting is produced both at the conduction band maximum (CBM) and the valence band minimum (VBM). We call the valley splitting at CBM as VS1, defined as VS1 =

TABLE I. The band gaps (BG) and the VS1 and the VS2 values of CrOCl and CrOBr, respectively.

	$\mathrm{BG}_{\mathrm{PBE}}$ (eV)	$\mathrm{BG}_{\mathrm{HSE06}}$ (eV)	$\mathrm{VS1}_{\mathrm{PBE}}$ (meV)	$\mathrm{VS1}_{\mathrm{HSE06}}$ (meV)	$\mathrm{VS2}_{\mathrm{PBE}}$ (meV)	$\mathrm{VS2}_{\mathrm{HSE06}}$ (meV)
CrOCl	0.703	3.233	33	100	8	7
CrOBr	0.650	2.079	54	112	44	–

E_K–$E_{K'}$, and the valley splitting at the VBM as VS2, defined as VS2 = E_A–$E_{A'}$. The band dispersion relationship over the entire Brillouin zone is shown in Fig. 1(a). CrOBr has bigger valley splitting than that of CrOCl, and the VS1 and VS2 in CrOBr reach to 52 and 44 meV, respectively. To obtain a more accurate band structure, we also do calculations by using the HSE06 function, and find that the VS1 increases to 100 and 112 meV for CrOCl and CrOBr, respectively, as shown in Fig. S6 of the SM [45]. However, the VS2 of CrOCl do not change and the VS2 of CrOBr is obliterated. The detailed information is shown in Table I.

We further analyze the intrinsic mechanism of the valley splitting generation. Due to the single spin polarization state, we neglect the interaction between the spin-up and spin-down states, and the Hamiltonian of spin-orbit coupling can be written as [51,52]

$$\begin{aligned}\hat{H}_{\mathrm{SOC}} &\approx \hat{H}^{0}_{\mathrm{SOC}}\\ &= \lambda \hat{S}_{z'}\left(\hat{L}_z\cos\theta+\frac{1}{2}\hat{L}_+\,e^{-i\emptyset}\sin\theta+\frac{1}{2}\hat{L}_-e^{+i\emptyset}\sin\theta\right),\end{aligned} \tag{3}$$

where $\hat{L}$ and $\hat{S}$ represent the orbital angular momentum and the spin angular momentum; (x, y, z) and (x', y', z') are the coordinate systems of $\hat{L}$ and $\hat{S}$, respectively. θ is the magnetocrystalline angle and it is zero along the z direction.

$$\hat{L}_+ = \hat{L}_x + i\hat{L}_y, \quad \hat{L}_- = \hat{L}_x - i\hat{L}_y. \tag{4}$$

The VBM is mainly contributed from d_{z^2} of Cr, while CBM is mainly contributed from $d_{x^2-y^2}$, d_{zy}, d_{xy}, and d_{zx} [as shown in Figs. 2(b) and 2(d)]. Since the symmetry group of the points K and K' (A and A') are C_{3h}, accordingly, the basic functions are $|\psi_v\rangle = |d_{z^2}\rangle$, $|\psi_c^\tau\rangle = \sqrt{\frac{1}{2}}(|d_{x^2-y^2}\rangle + i\tau|d_{xy}\rangle$, where $\tau = \pm 1$ represents the valley index. Therefore, the energy levels of the valleys at VBM and CBM are

$$E_v = \langle\psi_v|\hat{H}_{\mathrm{SOC}}|\psi_v\rangle, \quad E_c^\tau = \left\langle\psi_c^\tau\middle|\hat{H}_{\mathrm{SOC}}\middle|\psi_c^\tau\right\rangle. \tag{5}$$

Therefore, the energy difference between the two valleys is given by

$$\begin{aligned}&E_c - {E'}_c = i\langle d_{x^2-y^2}|\hat{H}_{\mathrm{SOC}}|d_{xy}\rangle - i\langle d_{xy}|\hat{H}_{\mathrm{SOC}}|d_{x^2-y^2}\rangle,\\ &E_v - {E'}_v \approx 0.\end{aligned} \tag{6}$$

From the above formulas, it can be found that spin-orbit coupling causes the breaking of the valley degeneration at the CBM, while the valley degeneration at the VBM is nearly not broken. These results are consistent with the band structure calculations with HSE06. Meanwhile, the basic functions $|d_{x^2-y^2}\rangle$ and $|d_{xy}\rangle$ are given by

$$\begin{aligned}|d_{x^2-y^2}\rangle &= \frac{1}{\sqrt{2}}(|d_{+2}\rangle + |d_{-2}\rangle),\\ |d_{xy}\rangle &= \frac{1}{\sqrt{2}}[-i(|d_{+2}\rangle + |d_{-2}\rangle)].\end{aligned} \tag{7}$$

Then, we can obtain $E_c - {E'}_c \propto 4\cos\theta$, which means that the valley splitting will vary as the cosine function of the magnetocrystalline angle. These results are consistent with our calculations from the first principles, as shown in Figs. 3(a) and 3(b). Subsequently, the magnetic anisotropy energies (MAEs) of CrOCl and CrOBr, which are defined as $\mathrm{MAE}(\theta) = E_\theta - E_0$, are also studied, as shown in Figs. 3(c) and 3(d). The MAEs have an angular dependence in the xz plane. Also, both of them prefer out of plane magnetization, which is more prone to valley splitting than the case with in-plane magnetization.

The valley splitting can give rise to AVHE in CrOCl and CrOBr. To demonstrate this, we calculate the Berry curvature from Kubo formula derivation,

$$\Omega(\boldsymbol{k}) = -\sum_{n}\sum_{n'\neq n} f_n \frac{2\,\mathrm{Im}\langle\varphi_{nk}|v_x|\varphi_{n'k}\rangle\langle\varphi_{nk}|v_y|\varphi_{n'k}\rangle}{(E_n - E_{n'})^2}, \tag{8}$$

where f_n is the Fermi-Dirac distribution function and $v_{x(y)}$ is the velocity operator; φ_n is the Bloch wave function with eigenvalue E_n. The Berry curvatures show opposite signs and different absolute values at the K and K' valleys both in CrOCl and CrOBr, as shown in Figs. 4(a) and 4(b), which leads to AVHE. The Bloch electrons will acquire an anomalous velocity $v_\perp \sim E \times \Omega_z(k)$ in a transverse electric field if the valley splitting appears at the CBM [53]. By doping electrons, we can shift the Fermi level to the K' valley of the CBM, and the spin-up electrons from K' will accumulate on one side of the sample and acquire an AVHE. Meanwhile, the energy band structures of CrOCl and CrOBr near the Fermi energy level are fitted well with the Wannier function, and are shown in Figs. 4(c) and 4(d).

Next, we investigate the tunability of the valley splitting of CrOCl and CrOBr. The use of hydrostatic pressure or nonconducting atomic force microscopy allows the application of adjustable local pressure on the sample. Therefore, the biaxial strain can be applied to the crystal to manipulate the valley splitting. According to Fig. 5(a), we find that neither VS1 nor VS2 of CrOCl varies more than 2 meV over the biaxial strain range of −6% to 6%, and the valley splittings of CrOCl are robust to the biaxial strain. However, according to Fig. 5(b), we find that VS1 of CrOBr increases almost linearly with the increasing of the biaxial strain, while VS2 decreases with the increasing of the biaxial strain and VS2 has a switching response at a compressive strain of 4%. As shown in Fig. S8 of the SM [45], the atom-projected band structures under biaxial strain show that the contributions to the VBM from the Cr

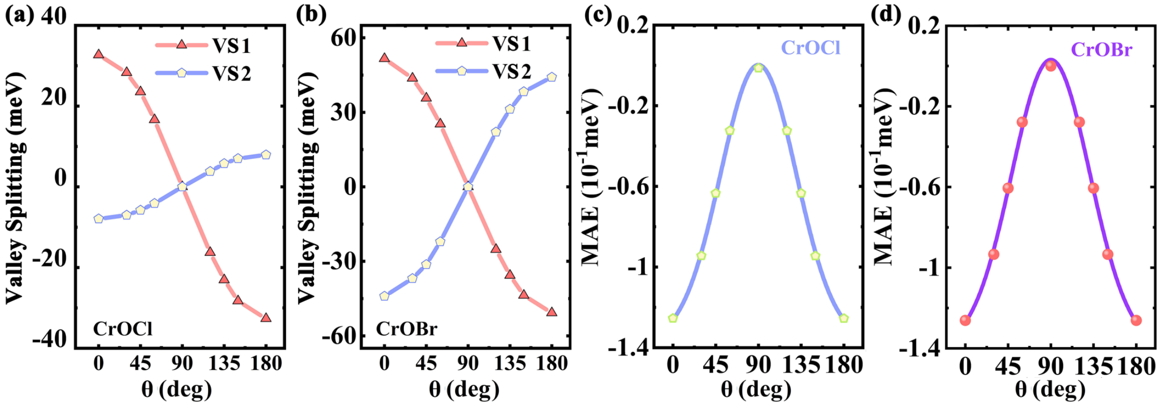

FIG. 3. (a), (b) are the VS1 and VS2 curves of CrOCl and CrOBr with different magnetocrystalline angles. (c), (d) are the MAE curves of CrOCl and CrOBr with different magnetocrystalline angles. The E_0 is set to zero when $\theta = 90^\circ$.

atoms are gradually replaced by the contributions from the Cl and Br atoms when the compressive strain increases. For CrOBr, when the compressive strain is −4%, the VBM moves to the Γ point and the VS2 disappears. Therefore, the change of the hybridization between atoms under biaxial strain is the inducement of the switching response of the valley splitting in CrOBr. Meanwhile, we investigate the effect of biaxial strain on MAE, as shown in Fig. 5(c). It can be found that the MAEs of CrOCl and CrOBr are negative when the biaxial strain changes from −6% to 6%, which favors the generation of stable valley splitting. Then, we find that the response of MAE with biaxial strain for CrOBr is more pronounced than that of CrOCl, which corresponds to an obvious change of the valley splitting under different biaxial strain in CrOBr, while the valley splitting of CrOCl is almost constant. Meanwhile, in order to explore the stability of valley splitting under strong electron correlation effects, the band structures and the variation curves of valley splitting of CrOCl and CrOBr are calculated for different *U* values, as shown in Fig. S9 of the SM [45]. It can be seen that the band gaps of CrO*X* increase with the increasing of the *U* value. As shown in Fig. S9(b) of the SM [45], we find that the VS1 values of CrOCl and CrOBr increase with the increasing of the *U* value and they nearly become constant. The VS2 values of CrOCl and CrOBr are almost constant when the *U* values change, while the VS2 in CrOBr disappears at a *U* value of 5, which is consistent with the switching response of the valley splitting discussed above under different biaxial strain. Thus, both the robustness of valley splitting in CrOCl and the switching response of valley splitting in CrOBr are significant for valleytronic applications.

We also consider the combination of FV and FE materials to form a multiferroic vdW heterostructure, so the switch of valley splitting as well as the AVHE in CrOCl can also be assisted. We utilize a $\sqrt{7} \times \sqrt{7}$ CrOCl supercell and a 2 × 2 In_2Se_3 supercell to build the multiferroic vdW heterostructure CrOCl/In_2Se_3; the lattice mismatch between the two monolayers is 2.65%, which is defined as $\mu = \frac{2|a_1-a_2|}{|a_1+a_2|}$. After considering the mirror asymmetry of Janus CrOCl and the two different polarization directions (up and down) of In_2Se_3, four different stacking configurations are constructed, which are indexed by O/↓, O/↑, Cl/↑, and Cl/↓, as shown in Fig. 6(a). The binding energy is defined as $E_b = E_{tot} - E_{CrOCl} - E_{In2Se3}$, where E_{tot}, E_{CrOCl}, and E_{In2Se3} represent the energies of CrOCl/In_2Se_3, CrOCl, and In_2Se_3, respectively. The E_b of the four configurations are all negative, which confirms the stability of them. Observing the energy spin-projected band structures in Fig. 6(b), we find that O/↓ and Cl/↑ are semiconducting, while O/↑ and Cl/↓ are metallic. The valley splitting of O/↓ and Cl/↑ are elevated to 49 meV, while it is 33 meV in monolayer CrOCl; however, the valley properties are buried in O/↑ and Cl/↓. The atom-projected band structures are shown in Fig. S11 of the SM [45]. The O/↓ and Cl/↑ are type I heterostructures, and the bands near the Femi level are coming mainly from the spin-up channels of CrOCl. The O/↑ and

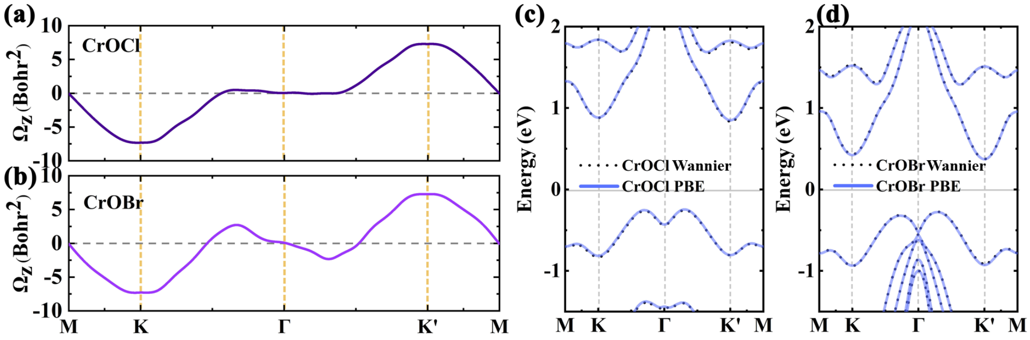

FIG. 4. (a), (b) are the Berry curvatures of CrOCl and CrOBr. (c), (d) are the band structures of CrOCl and CrOBr for PBE and Wannier function fitting, respectively.

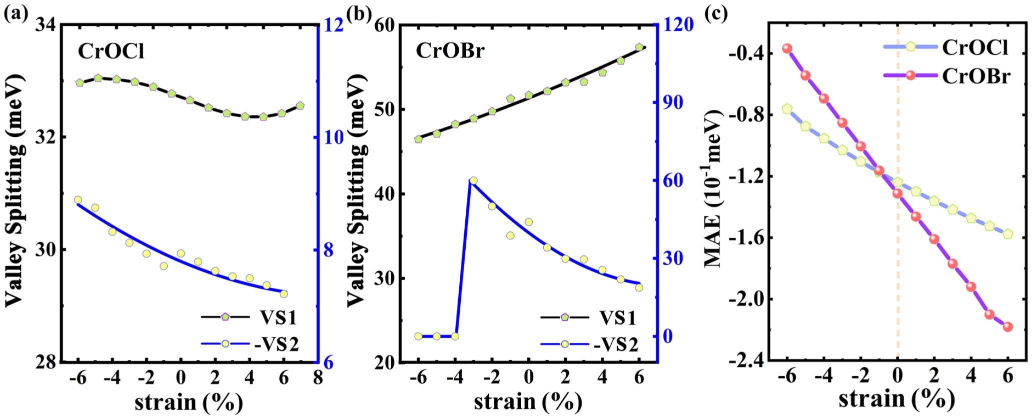

FIG. 5. (a), (b) are the valley splitting curves of CrOCl and CrOBr with different biaxial strain. (c) The MAE curves of CrOCl and CrOBr with different biaxial strain.

Cl/↓ are type III heterostructures, and the bands near the Femi level are coming both from CrOCl and In_2Se_3. Comparing Fig. S10 with Fig. S11 in the SM [45], it can be found that the spectral bands of the CrOCl/In_2Se_3 heterostructure are roughly similar to those of the corresponding monolayers, indicating that the hybridization between the monolayers is weak both for the up-polarization and the down-polarization cases. The polarization reversal only changes the band alignment and produces different heterostructure types, resulting in the submersion of the valleys or not. Therefore, we find that the polarization direction of the FE materials can control the electronic properties of the multiferroic heterostructure CrOCl/In_2Se_3 and thus the valley properties. After applying a short-term voltage on the multiferroic heterostructure, phase transition between up-polarization and down-polarization can be easily performed; then the ferroelectricity can be reversed, while the ferromagnetism remains unchanged, so reversible switching of valley splitting and AVHE can be achieved in the FV material. These will help to realize electrically read-write nonvolatile memory devices by using the duality of the valley degrees.

Due to the atomically thin nature of 2D materials, heterostructure interfaces play a very important role in the study of their properties. Using the proximity effect, the

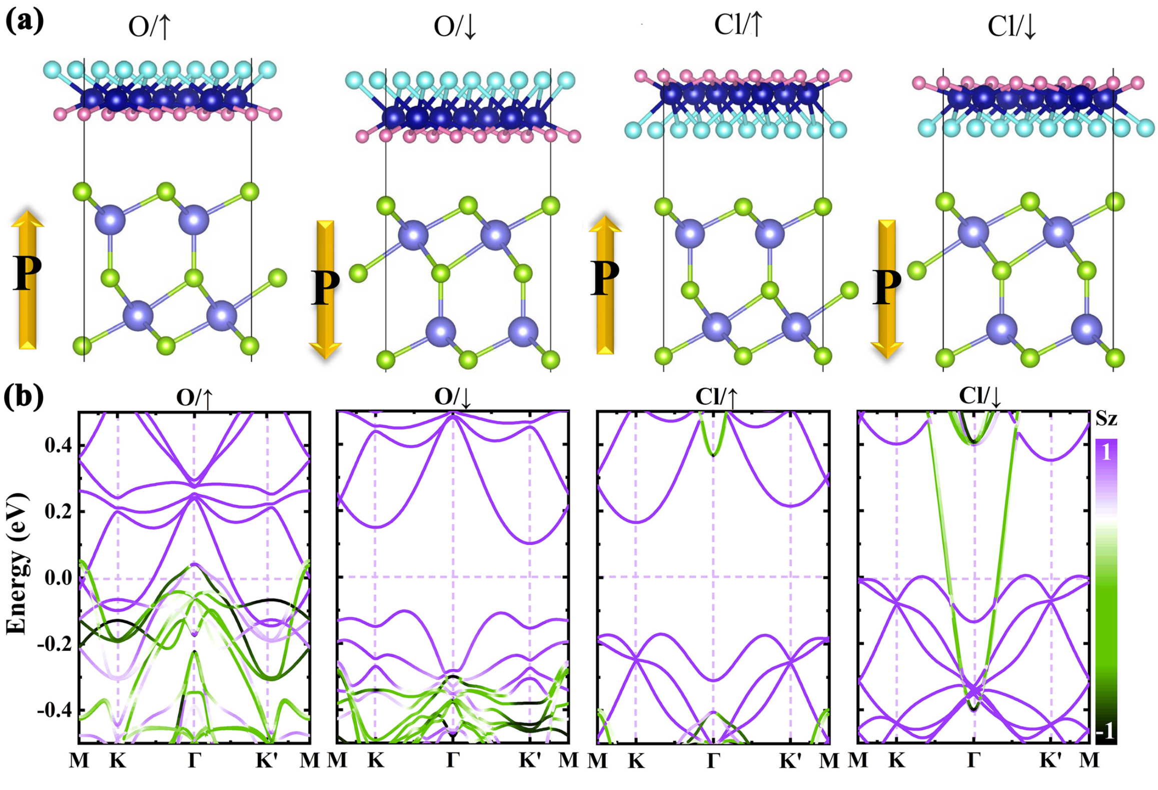

FIG. 6. (a) The structures of 2D vdW multiferroic heterostructure CrOCl/In_2Se_3 from side views for different configurations. $P\uparrow$ and $P\downarrow$ are the polarized states of FE material In_2Se_3. (b) The spin-projected band structures of the four stacking configurations.

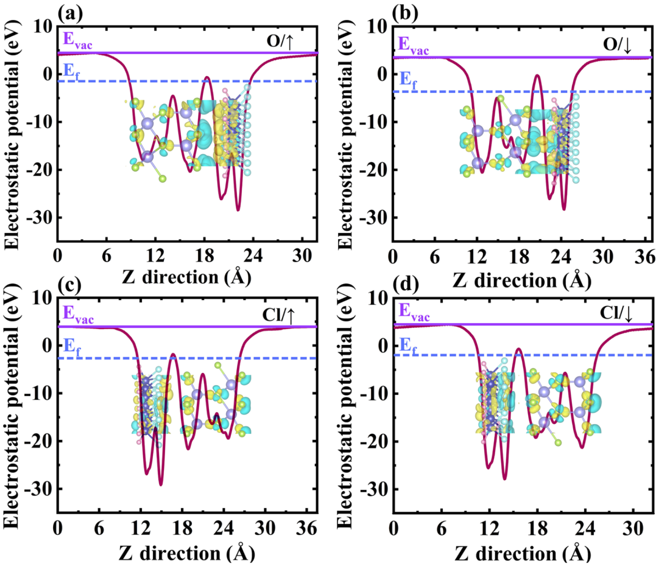

FIG. 7. (a)–(d) The electrostatic potentials and differential charge densities of the four stacking configurations.

polarized functional layer (FE materials) penetrates into the unpolarized channel layer (FV materials). A positive/negative surface bound charge dependent on the direction of the FE polarization is generated at the interface of the heterostructure. Electrons accumulate on one side of the polarized surface while holes accumulate on the other side, acquiring similar *p*-type/*n*-type semiconductors and thus playing a crucial role for the system's properties. Therefore, we further analyze the electrostatic potentials and the differential charge densities of the multiferroic heterostructure CrOCl/In$_2$Se$_3$, as shown in Figs. 7(a)–7(d). We find that when the direction of the built-in polarization field in Janus CrOCl is opposite to the polarization direction of the In$_2$Se$_3$ (O/↓ and Cl/↑), the electronic structures are semiconducting, and there is no electrostatic potential difference between the two ends of the heterostructures. On the contrary, the electronic structures are metallic for the cases of O/↑ and Cl/↓, while the electrostatic potential differences arise at both ends of the heterostructures. The system maintains its semiconductor nature due to the inhibition of interlayer charge transfer induced by the opposite directions of the polarizations. After reversing the polarization direction of the In$_2$Se$_3$, the charge transfer caused by the same electrolytic direction may lead to semiconductor to metal transition. The valley splitting switch and intervalley switching effects are achieved by applying a longitudinal short-term voltage.

The switch schematic of the AVHE under the action of an applied in-plane electric field is shown in Fig. 8. Figures 8(a) and 8(b) correspond to the switch-on of the AVHE. In Fig. 8(a) for the configuration of O/↓, the K' valley is lower than the K valley, so the carriers are only the Bloch electrons at the K' valley. After the in-plane electric field is applied, the Bloch electrons at K' are endowed with an anomalous transverse velocity, so they are transported only at the downward side of the device, while for the case of configuration of Cl/↑, the K valley is lower than that of the K' valley, so the Bloch electrons will be transported only at the upward side of the device. For Fig. 8(c) with the configurations of O/↑ and Cl/↓, the Bloch electrons have only the velocity obtained from the in-plane electric field, so the AVHE is switched off. The switch-on and switch-off of the AVHE can be achieved by changing the polarization direction of the FE materials or the stacking configurations in our constructed multiferroic vdW heterostructure CrOCl/In$_2$Se$_3$. The above results indicate that the AVHE reversible switch in this system has a promising application in the field of valleytronics.

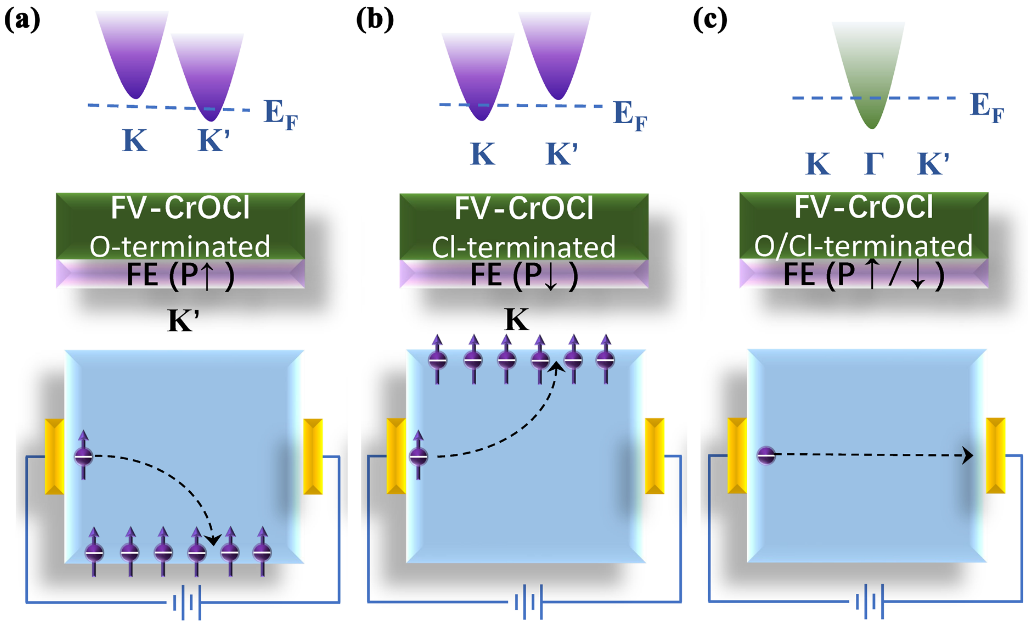

FIG. 8. The schematic of reversible switch of the AVHE under the action of an in-plane electric field.

IV. CONCLUDING REMARKS

In conclusion, we predict that monolayer Janus 1*T*-CrO*X* ($X = \mathrm{Cl}$, Br) are intrinsic FV semiconductors with sizable valley splitting and large out of plane MAE by first-principles calculations. Also, the valley splitting of CrOCl is robust to biaxial strain with variations below 2 meV both in the conduction band and the valence band, while the valley splitting of CrOBr exhibits a switching response at the valence band due to the strong orbital hybridization induced by the compressive strain; then the reversible switching effect of the AVHE can be achieved. Meanwhile, it is experimentally difficult to apply an external electric field to achieve valley splitting and AVHE, so we utilize the nature of the controlling polarization direction of the FE materials to build a multiferroic heterostructure CrOCl/In_2Se_3. The valley splitting switch and the intervalley switching effects can be achieved by applying a longitudinal short-term voltage under the action of the applied in-plane electric field in the heterostructure. Therefore, we achieve reversible AVHE switching by applying biaxial strain or building multiferroic heterostructures, respectively. Our work provides unique ideas for the development of nonvolatile and reversible memory devices for valleytronics.

ACKNOWLEDGMENTS

This work was supported by the Natural Science Foundation of Shandong Province (Grant No. ZR2021MA105), the National Natural Science Foundation of China (Grants No. 11674197 and No. 11974215), and the Qingchuang Science and Technology Plan of Shandong Province (Grant No. 2019KJJ014).

[1] J. R. Schaibley, H. Yu, G. Clark, P. Rivera, J. S. Ross, K. L. Seyler, W. Yao, and X. Xu, Nat. Rev. Mater. **1**, 16055 (2016).
[2] X. Li, T. Cao, Q. Niu, J. Shi, and J. Feng, Proc. Natl. Acad. Sci. USA **110**, 3738 (2013).
[3] D. Xiao, W. Yao, and Q. Niu, Phys. Rev. Lett. **99**, 236809 (2007).
[4] H. Zeng, J. Dai, W. Yao, D. Xiao, and X. Cui, Nat. Nanotechnol. **7**, 490 (2012).
[5] G. Kioseoglou, A. Hanbicki, M. Currie, A. Friedman, D. Gunlycke, and B. Jonker, Appl. Phys. Lett. **101**, 221907 (2012).
[6] A. Kareekunnan, M. Muruganathan, and H. Mizutaab, Nanoscale **11**, 14707 (2019).
[7] D. Gunlycke and C. T. White, Phys. Rev. Lett. **106**, 136806 (2011).
[8] A. Zhang, K. K. Yang, Y. Zhang, A. L. Pan, and M. X. Chen, Phys. Rev. B **104**, L201403 (2021).
[9] T. Zhou, S. Cheng, M. Schleenvoigt, P. Schüffelgen, H. Jiang, Z. Q. Yang, and I. Žutić, Phys. Rev. Lett. **127**, 116402 (2021).
[10] K. F. Mak, K. He, J. Shan, and T. F. Heinz, Nat. Nanotechnol. **7**, 494 (2012).
[11] T. Cai, S. A. Yang, X. Li, F. Zhang, J. Shi, W. Yao, and Q. Niu, Phys. Rev. B **88**, 115140 (2013).
[12] R. Peng, Y. Ma, S. Zhang, B. Huang, and Y. Dai, J. Phys. Chem. Lett. **9**, 3612 (2018).
[13] R. J. Sun, J. J. Lu, X. W. Zhao, G. C. Hu, X. B. Yuan, and J. F. Ren, Appl. Phys. Lett. **120**, 063103 (2022).
[14] J. T. Guo, X. B. Yuan, X. W. Zhao, G. C. Hu, and J. F. Ren, Appl. Surf. Sci. **558**, 149604 (2021).
[15] X. L. Xu, Z. L. He, Y. Dai, B. B. Huang, and Y. D. Ma, Phys. Rev. B **104**, 205430 (2021).
[16] P. Jiang, L. Kang, Y. L. Li, X. Zheng, Z. Zeng, and S. Sanvito, Phys. Rev. B **104**, 035430 (2021).
[17] H. Hu, W. Y. Tong, Y. H. Shen, X. G. Wan, and C. G. Duan, Nat. Commun. **7**, 13612 (2016).
[18] H.-X. Cheng, J. Zhou, W. Ji, Y.-N. Zhang, and Y.-P. Feng, Phys. Rev. B **103**, 125121 (2021).
[19] Y. Zang, Y. Ma, R. Peng, H. Wang, B. Huang, and Y. Dai, Nano Res. **14**, 834 (2021).
[20] Y. Wang, W. Wei, H. Wang, N. Mao, F. Li, B. Huang, and Y. Dai, J. Phys. Chem. Lett. **10**, 7426 (2019).
[21] Z. Zhang, J. Y. You, B. Gu, and G. Su, J. Phys. Chem. C **124**, 19219 (2020).
[22] C. Zhang, Z. Sun, Y. Lin, L. Guan, and J. Tao, Phys. Chem. Chem. Phys. **22**, 11409 (2020).
[23] C. M. Zhang, Y. H. Nie, S. Sanvito, and A. J. Du, Nano Lett. **19**, 1366 (2019).
[24] X. W. Zhao, F. J. Liu, J. F. Ren, and F. Y. Qu, Phys. Rev. B **104**, 085119 (2021).
[25] S. D. Guo, J. X. Zhu, W. Q. Mu, and B. G. Liu, Phys. Rev. B **104**, 224428 (2021).
[26] Y. Cheng, Q. Zhang, and U. Schwingenschlögl, Phys. Rev. B **89**, 155429 (2014).
[27] J. Ding, Z. Qiao, W. Feng, Y. Yao, and Q. Niu, Phys. Rev. B **84**, 195444 (2011).
[28] H. Pan, Z. Li, C.-C. Liu, G. Zhu, Z. Qiao, and Y. Yao, Phys. Rev. Lett. **112**, 106802 (2014).
[29] H. Hu, W. Y. Tong, Y. H. Shen, and C. G. Duan, J. Mater. Chem. C **8**, 8098 (2020).
[30] C. G. Lei, X. L. Xu, T. Zhang, B. B. Huang, Y. Dai, and Y. D. Ma, J. Phys. Chem. C **125**, 2802 (2021).
[31] B. X. Zhai, R. Q. Cheng, W. Yao, L. Yin, C. H. Shen, C. X. Xia, and J. He, Phys. Rev. B **103**, 214114 (2021).
[32] P. Jiang, L. L. Kang, H. Hao, X. H. Zheng, Z. Zeng, and S. Sanvito, Phys. Rev. B **102**, 245417 (2020).
[33] P. E. Blöchl, Phys. Rev. B **50**, 17953 (1994).
[34] G. Kresse and D. Joubert, Phys. Rev. B **59**, 1758 (1999).
[35] G. Kresse and J. Furthmüller, Comput. Mater. Sci. **6**, 15 (1996).
[36] J. P. Perdew, K. Burke, and M. Ernzerhof, Phys. Rev. Lett. **77**, 3865 (1996).
[37] H. J. Monkhorst and J. D. Pack, Phys. Rev. B **13**, 5188 (1976).
[38] J. Heyd, G. E. Scuseria, and M. Ernzerhof, J. Chem. Phys. **118**, 8207 (2003).
[39] D. Hobbs, G. Kresse, and J. Hafner, Phys. Rev. B **62**, 11556 (2000).
[40] S. L. Dudarev, G. A. Botton, S. Y. Savrasov, C. J. Humphreys, and A. P. Sutton, Phys. Rev. B **57**, 1505 (1998).

[41] S. Grimme, J. Antony, S. Ehrlich, and S. Krieg, J. Chem. Phys. **132**, 154104 (2010).

[42] S. Baroni, S. D. Gironcoli, A. D. Corso, and P. Giannozzi, Rev. Mod. Phys. **73**, 515 (2001).

[43] A. A. Mostofi, J. R. Yates, G. Pizzi, Y.-S. Lee, I. Souza, D. Vanderbilt, and N. Marzari, Comput. Phys. Commun. **185**, 2309 (2014).

[44] R. F. Evans, W. J. Fan, P. Chureemart, T. A. Ostler, M. O. Ellis, and R. W. Chantrell, J. Phys.: Condens. Matter **26**, 103202 (2014).

[45] See Supplemental Material at http://link.aps.org/supplemental/10.1103/PhysRevB.105.235416 for more details on the electronic, mechanical, and magnetic properties of the systems.

[46] Y. Ren, Q. Li, W. Wan, Y. Liu, and Y. Ge, Phys. Rev. B **101**, 134421 (2020).

[47] V. Wang, N. Xu, J. C. Liu, G. Tang, and W. T. Geng, Comput. Phys. Commun. **267**, 108033 (2021).

[48] J. B. Goodenough, Phys. Rev. **100**, 564 (1955).

[49] J. Kanamori, J. Phys. Chem. Solid **10**, 87 (1959).

[50] B. Huang, G. Clark, E. Navarro-Moratalla, D. R. Klein, R. Cheng, K. L. Seyler, D. Zhong, E. Schmidgall, M. A. McGuire, D. H. Cobden, W. Yao, D. Xiao, P. Jarillo-Herrero, and X. Xu, Nature (London) **546**, 270 (2017).

[51] R. Peng, Y. Ma, X. Xu, Z. He, B. Huang, and Y. Dai, Phys. Rev. B **102**, 035412 (2020).

[52] M.-H. Whangbo, E. E. Gordon, H. Xiang, H.-J. Koo, and C. Lee, Acc. Chem. Res. **48**, 3080 (2015).

[53] D. Xiao, M. C. Chang, and Q. Niu, Rev. Mod. Phys. **82**, 1959 (2010).